J. Fluid Mech. (1996), vol. 324, pp. 83–108

Three-dimensional separated flow structure over a cylinder with a hemispherical cap

By T. HSIEH[1] AND K. C. WANG[2]

[1] Information Sciences and Systems Branch, Naval Surface Warfare Center, Silver Spring, MD 20903, USA

[2] Aerospace Engineering and Engineering Mechanics, San Diego State University, San Diego, CA 92182, USA

(Received 1 July 1994 and in revised form 20 February 1996)

Thin-layer Navier–Stokes solutions are obtained for an incompressible laminar flow over a hemisphere–cylinder at 10°, 30° and 50° incidence to exhibit some three-dimensional separated flow characteristics. Some of the results are compared with a previous water-tunnel investigation for the same body geometry. Good agreement is found, even for some detailed features. Although the geometry is relatively simple, the separated flow surprisingly embraces a number of intricate structural characteristics unique to three-dimensional flows. Particularly noteworthy are the separation sequence at increasing incidence, tornado-like vortices, outward-spiralling vortices, limit cycles, coaxial counter-spiralling patterns and horseshoe vortex systems. Physical insights to these new features are offered.

1. Introduction

Very few three-dimensional separated flows have been thoroughly investigated. In this work numerical solutions of the incompressible laminar Navier–Stokes flow over a cylinder with a hemispherical end are reported to demonstrate some pertinent features. Although this particular geometry is relatively simple, the flow structure found surprisingly embraces intricate new three-dimensional patterns.

Since the present authors reported the appearance of a tornado-like concentrated nose vortex in the fore-body of a hemisphere–cylinder (Hsieh & Wang 1976; Hsieh 1976, 1977), there have been a number of attempts to calculate this separated flow problem (Pulliam & Steger 1980; Hsieh 1981; Tobak & Peake 1982; Kordulla, Vollmers & Dallmann 1986; Ying *et al.* 1986; Ying, Schiff & Steger 1987). Although there have been considerable advances in the understanding of this problem in the transonic range, a systematic study of the separation pattern and flow structure at low to high incidence has not been reported.

In 1989, Wang, Hu & Zhou reported extensive water-tunnel experiments on a hemisphere-cylinder at incidences from 0° to 90°. Two different techniques were used: (i) paint coating and point dots and (ii) dye injection. The former was used to show the flow characteristics on the body surface, the latter above the body surface. The paints used were the usual poster paints. Paint coating shows sharp separation lines, whereas paint dots are effect in exhibiting the flow pattern inside the separated region. This paint coating and dots method was first reported by Wang *et al.* (1990); it is analogous to the classical oil coating and oil dots used in a wind tunnel. Dye injection is a classical method of producing streaklines. The dye used was food colouring mixed with glue in

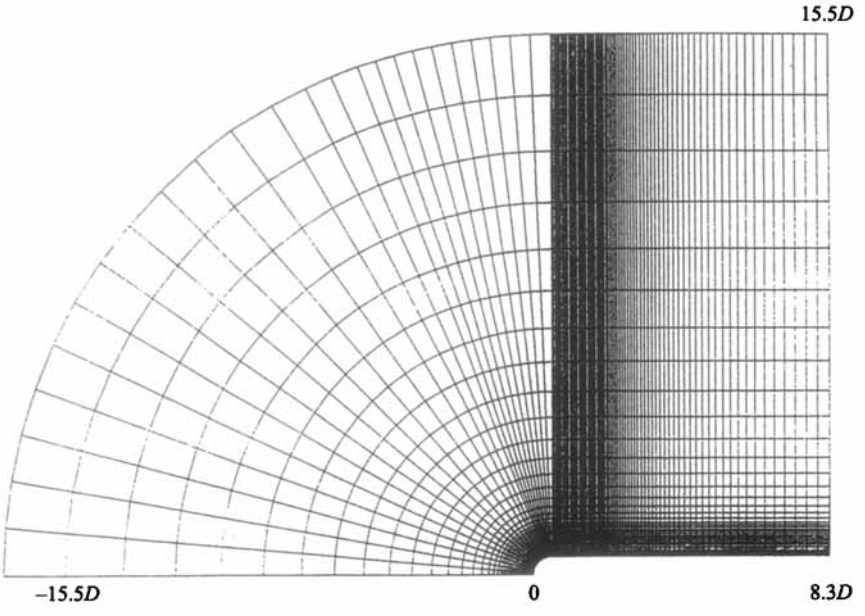

FIGURE 1. Computational grid and domain.

order to slow the diffusion. All the photos of the experiments were originally taken in colour, but reproduced later in black and white for journal publication.

The experimental results established a systematic separation trend. As the incidence increases, the separated flow in the nose region becomes rather complicated. Of particular interest is the sequence of the change of separation pattern from an open type to a closed type on the body surface and the formation of tornado-like vortices and horseshoe vortex systems.

The present computational investigation is intended to be a parallel effort to check, in part, most of the experimental findings wherever applicable and to add further detailed flow field structure away from the body surface. Parts of preliminary results were reported at an AIAA conference (Wang & Hsieh 1992).

Numerical methods are presented in §2 and results in §3. In §4, a number of new features are highlighted, and possible explanations are attempted to give insight into why and how they occurred. Certain aspects, however, remain not well understood and need further investigation.

2. Numerical procedures

A brief description of the numerical procedures and code used in this calculation is given here. The numerical code used is CFL3D developed by Thomas, Krish & Anderson (1990, see also Van Leer *et al.* 1987). For a detailed description of the numerical algorithm and definition of the symbols, the reader should consult the original work. The governing equations are the single/double thin-layer approximations to the three-dimensional time-dependent compressible Navier–Stokes equations, written in generalized coordinates (ξ, η, ζ) and conservation form as follows:

$$\frac{\partial}{\partial t}(\boldsymbol{Q})+\frac{\partial}{\partial \xi}(\boldsymbol{F})+\frac{\partial}{\partial \eta}(\boldsymbol{G}-\boldsymbol{G}_v)+\frac{\partial}{\partial \zeta}(\boldsymbol{H}-\boldsymbol{H}_v)=0, \tag{1}$$

where $\boldsymbol{Q}=(J^{-1})\ (\rho, \rho u, \rho v, \rho w, e)^T$, $\boldsymbol{F}$, $\boldsymbol{G}$, $\boldsymbol{H}$ are the inviscid flux vectors and the

subscript v stands for the corresponding viscous flux vectors, J is the Jacobian $\partial(\xi,\eta,\zeta)/\partial(x,y,z)$, ρ the density, e the total energy, and u, v, w are the x, y, z Cartesian velocity components. The equation of state for an ideal gas is used to define the pressure $p = (\gamma-1)[e-\rho(u^2+v^2+w^2)/2]$, where γ is the ratio of specific heats. Stokes' hypothesis for bulk viscosity and Sutherland's law for molecular viscosity are used to close the system. Since only laminar flows are considered in this paper, turbulent modelling is not required.

The flux difference splitting scheme of Roe (1981) is chosen for all the inviscid generalized fluxes $\boldsymbol{F}$, $\boldsymbol{G}$ and $\boldsymbol{H}$. For example, the flux difference in the ξ-direction at the ith cell is split into forward and backward contributions,

$$\left.\begin{aligned}(\partial \boldsymbol{F}/\partial\xi)_i &= \boldsymbol{F}_{i+1/2}-\boldsymbol{F}_{i-1/2},\\ \boldsymbol{F}_{i+1/2} &= \tfrac{1}{2}[\boldsymbol{F}(q^-)+\boldsymbol{F}(q^+)-|\boldsymbol{A}|(\boldsymbol{Q}^+-\boldsymbol{Q}^-)]_{i+1/2},\end{aligned}\right\} \tag{2}$$

where $q^{\pm}$ denotes state variables on a cell interface, and $\boldsymbol{A} = \partial\boldsymbol{F}/\partial\boldsymbol{Q}$ is the averaged value at cell interface. The diffusion terms are treated using a central difference scheme while the linearized backward-time approximation in delta form is used for the time differencing. When treated with the spatially factored scheme, the three-dimensional equations are solved by a series of sweeps through the three directions as follows:

$$\left.\begin{aligned}&\left[\frac{\boldsymbol{I}}{J\Delta t}+\delta_\zeta\left(\frac{\partial \boldsymbol{H}}{\partial \boldsymbol{Q}}-\frac{\partial \boldsymbol{H}_v}{\partial \boldsymbol{Q}}\right)\right]\Delta\boldsymbol{Q}^* = -L(\boldsymbol{Q}^n),\\ &\left[\frac{\boldsymbol{I}}{J\Delta t}+\delta_\eta\left(\frac{\partial \boldsymbol{G}}{\partial \boldsymbol{Q}}-\frac{\partial \boldsymbol{G}_v}{\partial \boldsymbol{Q}}\right)\right]\Delta\boldsymbol{Q}^{**} = \left(\frac{\boldsymbol{I}}{J\Delta t}\right)\Delta\boldsymbol{Q}^*,\\ &\left[\frac{\boldsymbol{I}}{J\Delta t}+\delta_\xi\left(\frac{\partial \boldsymbol{F}}{\partial \boldsymbol{Q}}\right)\right]\Delta\boldsymbol{Q} = \frac{\boldsymbol{I}}{J\Delta t}\Delta\boldsymbol{Q}^{**},\\ &\boldsymbol{Q}^{n+1} = \boldsymbol{Q}^n+\Delta\boldsymbol{Q},\end{aligned}\right\} \tag{3}$$

where $-L(\boldsymbol{Q}^n)$ is the discrete representation of the spatial derivative terms in (1) evaluated at time level n. The algorithm is written in delta form so that the steady-state solution is independent of time step Δt. The implicit spatial derivatives for the convective and pressure terms are first-order accurate. This leads to the block tri-diagonal solution. Second-order-accurate upwind-biased spatial differencing is maintained for the residual calculation producing a second-order steady-state solution.

The computational domain for the hemisphere–cylinder calculation is shown in figure 1 where the body surface, the singular axis, the far-field inflow boundary, and the outflow plane are shown. Boundary conditions are explicitly implemented. On the body surface no-slip, no penetration and isothermal wall conditions are imposed. For the singular axis, a continuation of cell centre flow variables are imposed. At the far-field inflow boundary, the free-stream condition holds. At the outflow plane, a zero gradient of flow quantities is implemented. The flow is assumed to be symmetrical with respect to the pitching plane, so only half of the cross-flow plane needs to be computed. The initial conditions are uniform free-stream conditions everywhere with $u = v = w = 0$ on the solid boundary.

Two different grids were used in the computation: one for 10° incidence (figure 1) with grids 101 (axial) × 69 (circumferential) × 51 (radial), the other for 30° and 50° incidence with grids 101 × 68 × 75. In the axial direction, grid points were concentrated more in the nose region where the flow varies most. In the circumferential direction, a constant grid spacing of 2° was used between the leeward plane, $\theta = 0°$, and $\theta = 100°$, followed by a smooth increase to 5° at $\theta = 110°$. The circumferential grid spacing remained constant from this point to the windward side, $\theta = 180°$. In the radial

direction, the minimum grid spacing above the body surface was $0.000\,15D$, where D is the cylinder diameter.

All calculations were carried out using the NAS Cray II/YMP supercomputer located at NASA Ames Research Center. A steady-state solution was reached when the lift coefficient was essentially constant over a few hundred time iterations. This usually took 3000 to 5000 time steps.

3. Results

The computer program was written for compressible flows. The present calculation was carried out with Mach number equal to 0.2 in order for the flow to be considered approximately as incompressible and hence enable comparison with water-tunnel experiments (Wang *et al.* 1989). The Reynolds number was 1.4×10^4 based on the cylinder diameter. Three different incidences, $\alpha = 10°$, 30°, 50°, were calculated. Particle trace plots were made using PLOT3D (Walatka *et al.* 1990). The direction of flow is from right to left.

How to present three-dimensional results in order to effectively project three-dimensional structures is a difficult task in itself. Traditionally, three-dimensional flows have been presented along the symmetry-plane and at different cross-planes. In this paper, we have extended this to include views on parallel surfaces and at meridional planes (in addition to the symmetry one). These are still all two-dimensional in nature. Some particle tracings are also included; they are genuine three-dimensional plots.

These two-dimensional views are convenient to make from both experiments and calculations. In experiments, the cut-plane views are made visible by a plane sheet light which illuminates a particular plane section. From calculations, two-dimensional views can be obtained by neglecting the velocity component normal to the plane or curved surface concerned. The two-dimensional views do not represent physical flows except those in the symmetry plane or on the body surface. However, if a series of such two-dimensional views are stacked one on top of another, they do project a three-dimensional flow picture even though one would have difficulty in drawing such a picture. Drawing of three-dimensional objects is inherently difficult; it is an art as much as a science.

Improvement of three-dimensional flow presentations could be forthcoming in two ways: (i) extension of the phase-plane topology to three-dimensional phase-space, and (ii) computer graphics. The usefulness of the phase-plane theory in analysing two-dimensional flow patterns is well known, but for general three-dimensional cases it remains to be explored. Phase-space theory (Perry & Chong 1981) is presented in terms of eigenvalues and eigenvectors; actual implementation to a specific problem is not straightforward. A plot of the limiting-streamline pattern over a body completely determines the surface topology, but no similar plot could effectively do the same for three-dimensional structures. Computer graphics could make three-dimensional presentations easier. This is a fast-growing area and, hopefully, will soon be advanced enough for the present purpose.

3.1. *10° incidence*

Our presentation for this relatively low incidence will be limited to the surface flow pattern, omitting the other details in order to reduce the length of this paper. The omitted details for the present 10° incidence contain less new features than the cases of $\alpha = 30°$ and 50°.

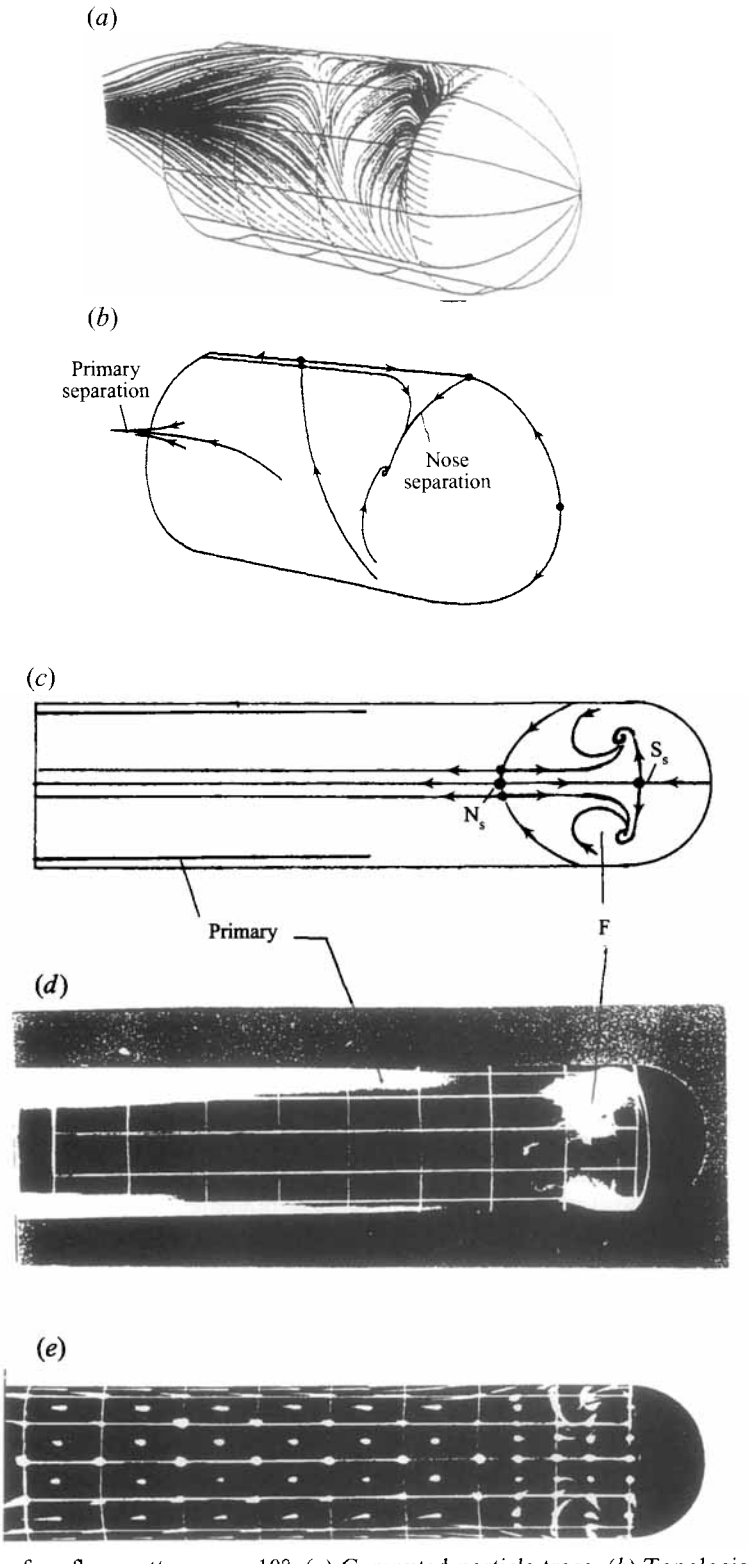

FIGURE 2. Surface flow pattern, $\alpha = 10°$. (*a*) Computed particle trace. (*b*) Topological sketch. (*c*) Redrawing of (*b*), (*d*, *e*) experiments.

Figure 2(*a*) shows the computed surface flow pattern, figure 2(*b*) the topological structure, and figure 2(*c*) is a redrawing of figure 2(*b*) for the convenience of comparison with experiments in figures 2(*d*, *e*). Over the cylinder portion, figure 2(*a*, *b*) shows that the limiting streamlines converge to form the primary separation line starting approximately at $x/D = 2.25$. There is no secondary separation except near the very rear end ($x/D = 5.5$).

In the meantime, the flow separates at the nose region; this nose separation ends in a pair of tornado-like vortices, which are characterized by their axis of rotation being inclined to the body surface. This will be elaborated in §4.1.

The calculated patterns are compared with experiments shown in figure 2(*d*, *e*): figure 2(*d*) clearly defines the separation lines, while the dots pattern of (figure 2*e*) provides more details behind separation. Good agreement is found not only in general trends regarding the nose separation line, tornado-like vortices, the primary separation line and the absence of the secondary separation, but also in quantitative comparisons for a few specific locations listed in table 1.

3.2. *30° incidence*

3.2.1. *Parallel-surface flow pattern*

Figure 3(*a*) shows the pressure distribution. At 30° incidence, the meridional gradient at the forebody and circumferential gradient over the cylinder are large, causing stronger separations.

Various parallel surfaces are defined by the number of computation steps k along the direction normal to the body; $k = 1$ denotes the body surface itself. Figure 3(*b*) shows the computed surface flow separation pattern, and figure 3(*c*) the topological structure; figure 3(*d*) is a redrawing of figure 3(*c*) for the convenience of comparing with the experimental pictures (figure 3*e*, *f*).

The separated flow structure in the nose region is most complex at $\alpha = 30°$. there are two stages of nose separation, marked I and II, across the symmetry-plane; both are basically of the axial-flow separation. The first occurs at $S_{s1}(x/D \approx 0.35)$ and reattaches at $N_{a1}(x/D \approx 1.3)$. The second occurs at $S_{s2}(x/D \approx 0.63)$ and is immediately reattached at $N_{a2}(x/D \approx 0.52)$. Each of these two separation lines ends in a pair of tornado-like vortices F_1 and F_2. All these latter vortices draw fluid partly from the upstream flow and partly from the two stages of separation I and II. Between them there seem to be two additional ones, separation III, one on each side of the symmetry-plane.

Over the cylindrical aftbody, there are the primary and secondary separation lines, both essentially of the nature of the cross-flow separation. The primary separation line starts at $x/D \approx 1.3$ and runs close to the meridional line $\theta \approx 90°$, the secondary line starts at $x/D \approx 1.9$ and runs close to the line $\theta = 30°$. Both are of the open type.

The corresponding experiments (Wang *et al.* 1989) are shown in figure 3(*e*, *f*). Figure 3(*d*, *e*) clearly shows the nose separation lines I and II, as well as the primary and secondary separation lines. Figure 3(*f*) is locally enlarged to display these two pairs of tornado-like vortices. Agreement over the surface flow is again found good in both general trends and quantitative comparison of specific locations, as listed in table 2.

The good agreement for the $\alpha = 30°$ case is especially significant because of the unusually complicated structure involved. It certainly enhances the validity of both calculations and experiments: otherwise it would be difficult to accept the complex patterns shown either in figure 3(*b*) from computer plots or topological sketches based on experiments in figure 3(*e*,*f*) without skepticism. The separation III is not revealed in figure 3(*e*,*f*) and hence remains to be confirmed.

Point $(x/D, \theta)$	S_s	N_a	F	SP1	SP2
Calculation	0.4	1.5	0.5, 60°	2.25, 60°	5.5, 40°
Experiment	0.4	1.5	0.70, 50°	2.2, 60°	NA

TABLE 1. Comparison for $\alpha = 10°$. SP1, SP2 refer to the starting points of the primary and secondary separation lines; other points are defined on figure 2. NA, denotes not available

Figure 3(*g*, *h*) shows the flow patterns on the parallel surfaces $k = 4$ and $k = 8$. Above the body, the second stage of separation II and its associated tornado-like vortices F_2 in the nose region quickly disappear. Meanwhile, vortex F_1 as well as the separation surface on the cylinder portion gradually shift toward the symmetry-plane, a trend also seen for $\alpha = 10°$ and 50°.

3.2.2. *Meridional-plane flow pattern*

The computer traces at the meridional planes $\theta = 0°$, 6°, 12°, 18° and 24°, together with their corresponding topological sketches are shown in figure 4(*a–e*).

The flow in the nose region of the symmetry plane $\theta = 0°$ (figure 4*a*) exhibits an unusually complex structure. It separates at S_{s1} and reattaches at N_{a1}. This separated flow ends up in vortex F_3. The second stage of separation, marked S_{s2} and N_{a2}, is very small in comparison. Of particular interest is the presence of a limit cycle. The details of this limit cycle are shown in the accompanying enlargement. Inside the limit cycle, there are two vortices, F_1 and F_2; F_1 is smaller and is fed with fluids from F_2. The vortices F_1 and F_3 spiral inward, whereas F_2 spirals outward. F_3 draws fluid from the incoming upstream flow, F_2 in contrast draws fluid laterally from the nose separated region. A limit cycle is usually characterized in the phase-plane literature as a closed curve which is approached by two different solutions, one from the outside and one from the inside. In the present case the limit cycle is approached by flows originated from two different sources, inside and outside.

Away from the symmetry plane, i.e. $\theta > 0°$, vortex F_3 disappears, but F_1 and F_2 persist. In the absence of F_3, the limit cycle also vanishes. Furthermore, the nose separation is not reattached in the back. This aspect occurs in the case of 10° incidence also.

3.2.3. *Cross-plane flow pattern*

The computer traces and corresponding topological sketches at selected cross-plane stations are shown in figure 5(*a–d*). They are chosen to display different variations. The pattern of figure 5(*a*) is typical at the forebody behind the nose separation. A nodal source point N_a appears on the leeside symmetry-plane and a cross-flow separation, S_{s1}, appears on the cylinder. At $x/D = 1.75$ (figure 5*b*), a vortex pattern is clearly developed. At $x/D = 3.50$ (figure 5*c*), the vortex of primary separation grows much larger, and a much smaller secondary separation S_{s2} also appears. Meanwhile a black area emerges in the core and persists all the way downstream.

The pattern shown in figure 5(*d*) at a farther downstream station, $x/D = 5.75$, is similar to that of figure 5(*c*) except for two aspects: the primary separation vortex regions is much larger, and a black ring appears in addition to the black core. Unlike the black core, this black ring does not persist long downstream: it appears and then quickly diminishes. This transitory condition could result from the discontinuous manner by which the fresh fluid is entrapped into the primary separation vortex. The

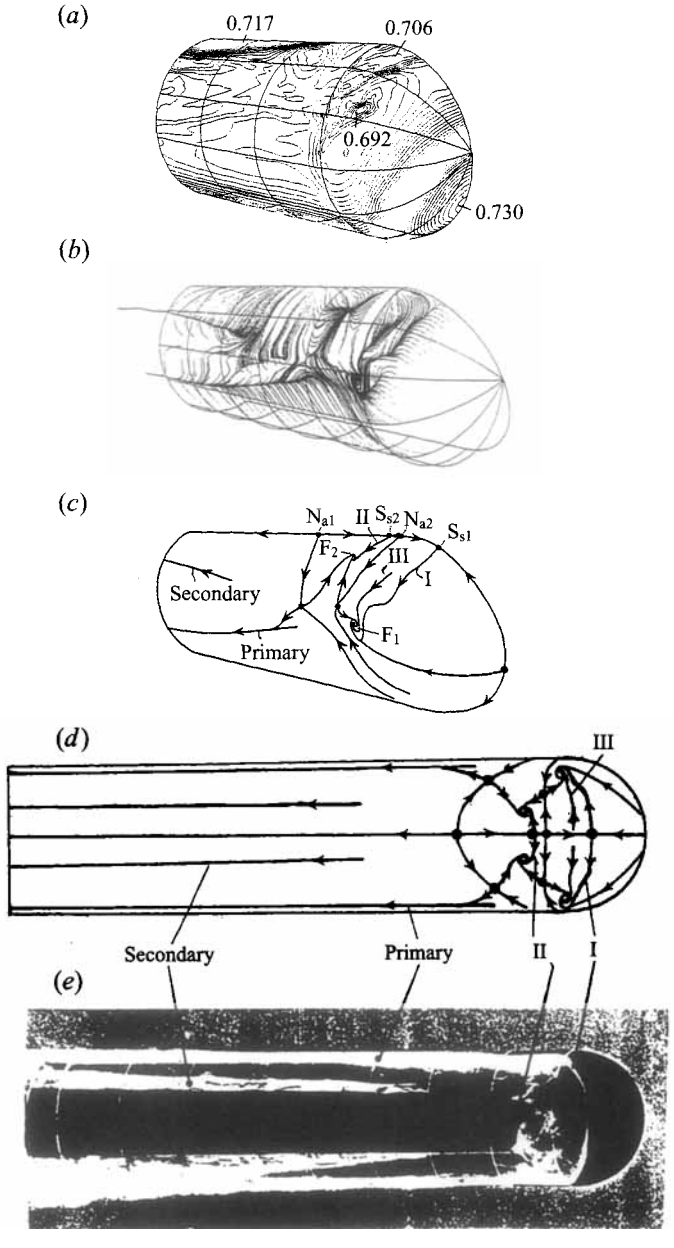

FIGURE 3(*a–e*). For caption see facing page.

cross-plane spiral motion and the meaning of the black core and black ring will be further elaborated in §§4.2 and 4.5.

The outward spiral vortices and the associated limit-cycle pattern in the cross-planes have been independently reported by Visbal & Gordnier (1994) in their delta-wings investigations and by Zhang & Deng (1992) and Zhang (1994) in their topological analysis of vortex motion. Zhang's works were unknown to the present authors until one of us (Wang) visited the China Aerodynamics Center in August 1995.

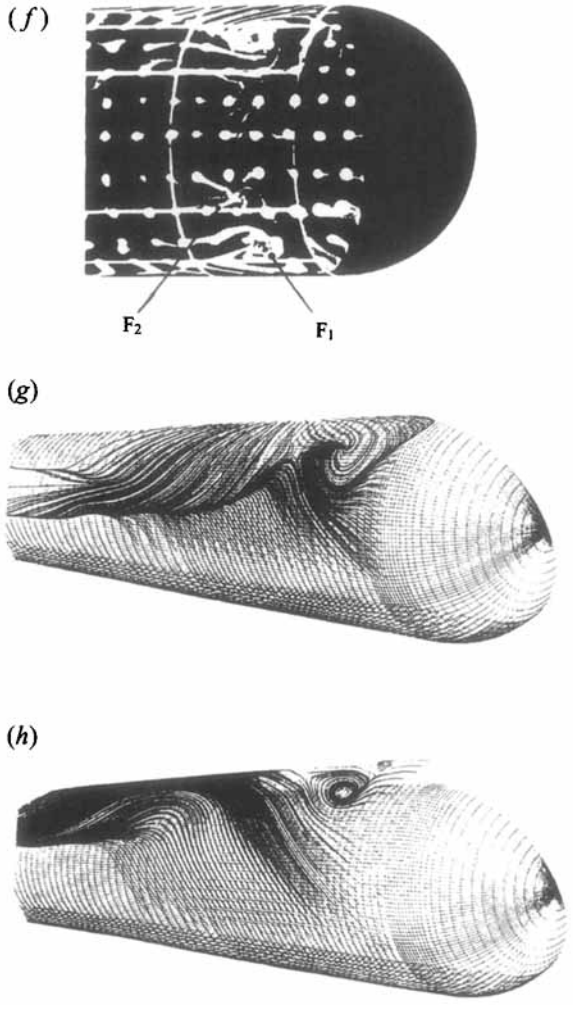

FIGURE 3. Parallel surface flow pattern, $\alpha = 30°$. (*a*) Surface pressure. (*b*) Computed particle trace, $k = 1$. (*c*) Topological sketch. (*d*) Redrawing of (*c*). (*e*,*f*) Experiments. (*g*, *h*) Parallel surface patterns; (*g*) $k = 4$, (*h*) $k = 8$.

Point $(x/D, \theta)$	S_{s1}	N_{a1}	S_{s2}	N_{a2}	F_1	F_2	SP1	SP2
Calculation	0.35	1.3	0.63	0.52	0.55, 62°	0.75, 20°	1.1, 70°	1.7, 45°
Experiment	0.30	1.3	0.75	0.50	0.72, 50°	0.80, 20°	1.1, 70°	NA

TABLE 2. Comparison for $\alpha = 30°$. SP1, SP2 denote starting points of primary and secondary cylinder separations. Other points are shown on figure 3(*c*)

3.3. *50° incidence*

3.3.1. *Parallel-surface flow pattern*

The surface pressure distribution (figure 6*a*) exhibits even larger gradients than that for $\alpha = 30°$, suggesting even stronger separation in both the meridional and circumferential directions.

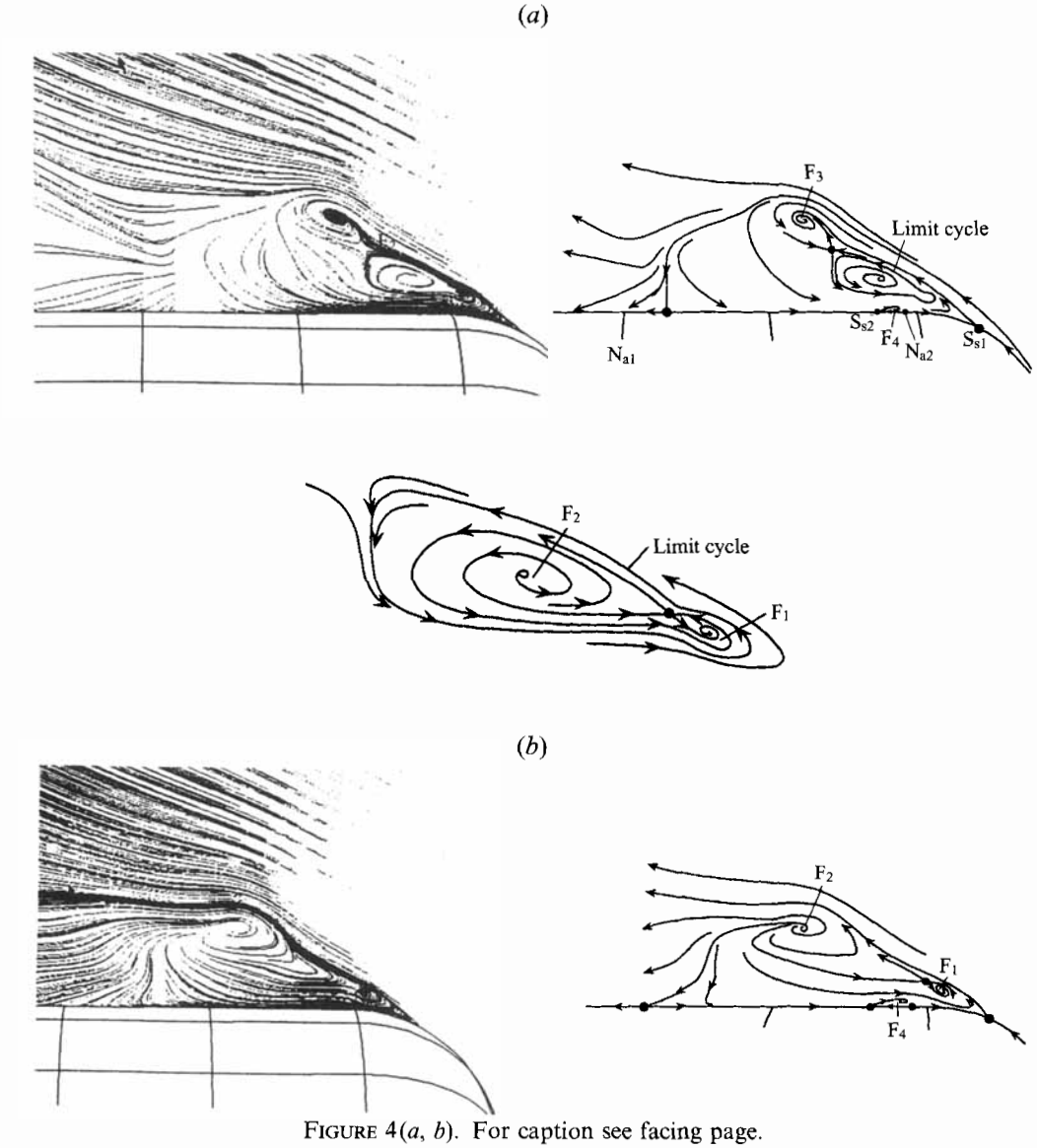

FIGURE 4(*a*, *b*). For caption see facing page.

Figure 6(*b*) shows the computed surface flow separation pattern, figure 6(*c*) the interpreted topological structure. Figure 6(*d*) is a redrawing of figure 6(*c*) to show the top view for comparison with experiments.

The surface flow separation pattern at $\alpha = 50°$ is very different from that of $\alpha = 30°$ and is less complicated. In the nose region there are still two stages of axial separation, but the first one is now connected to the primary separation over the cylinder portion, hence the surface flow separation pattern now becomes of closed type in contrast to the open type for $\alpha = 10°$ and 30°. Thus the pair of tornado-like vortices associated with this first stage of axial separation shown for $\alpha = 30°$ no longer exists here. This removes possible interactions between the tornado-like vortices and the nose separation vortex. As a result, the nose flow patterns would be more regular and less twisted than in the $\alpha = 30°$ case.

The remaining pair of tornado-like vorticies is associated with the second axial nose

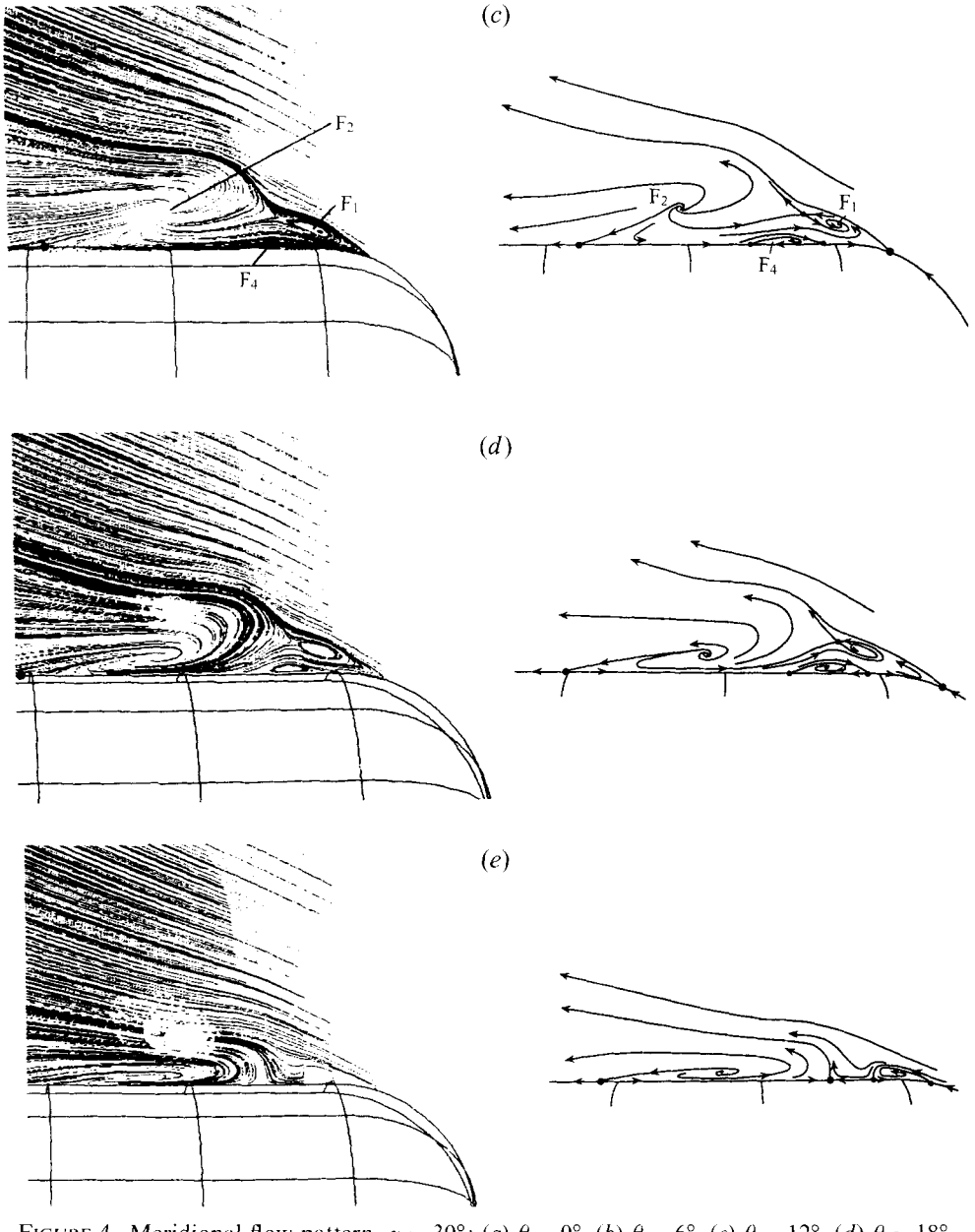

FIGURE 4. Meridional flow pattern, $\alpha = 30°$; (*a*) $\theta = 0°$, (*b*) $\theta = 6°$, (*c*) $\theta = 12°$, (*d*) $\theta = 18°$, (*e*) $\theta = 24°$.

separation; since these vortices are entirely inside the separated region, they do not draw fluid from the free upstream contrary to the preceding cases for $\alpha = 10°$ and $30°$. The tornado-like vortex for $\alpha = 50°$ is weaker than those for $\alpha = 10°$ and $30°$. Meanwhile, the secondary separation on the cylinder portion remains of the open type similar to the case for $\alpha = 30°$.

Figure 6(*e*) is the corresponding experimental picture. Agreement is found for features such as the curved shape of the nose separation, the closed type of primary separation and the open type of secondary separation.

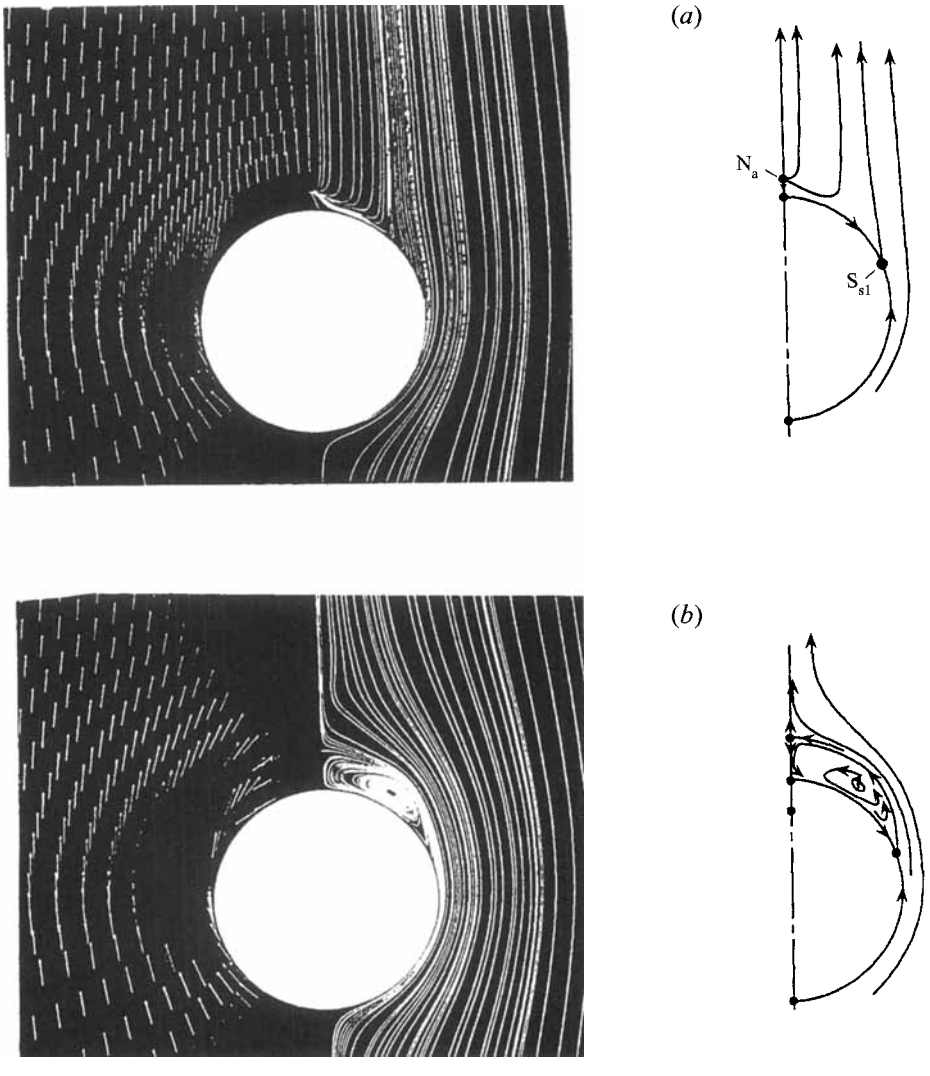

FIGURE 5(*a*, *b*). For caption see facing page.

Figure 6(*f*) shows the pattern on the parallel surface $k = 4$. Just as in the case of $\alpha = 30°$, the second axial nose separation quickly disappears above the body.

3.2.2. *Meridional-plane flow pattern*

The meridional-plane flow patterns are shown in figures 7(*a*), 7(*b*), and 7(*c*) for $\theta = 0°$, 12° and 24°. The nose separated structure is seen to be grossly different but simpler than that for $\alpha = 30°$. All the patterns are fairly consistent, always dominated by an outward-spiralling vortex F_2; the other vortex F_4, representing the second stage of axial nose separation, is fairly weak. The nose vortex represented by F_2 here is much stronger than those of figure 4(*a–e*) for $\alpha = 30°$. The upstream incoming flow separates at S_{s1}, but does not reattach at the back except for $\theta = 0°$, the same trend as noted in the preceding case of 30° incidence.

Figure 7(*d*, *e*) compares the calculated to the experimental symmetry-plane patterns. Figure 7(*d*) is an extended picture of figure 7(*a*); figure 7(*e*) is taken from the Masters

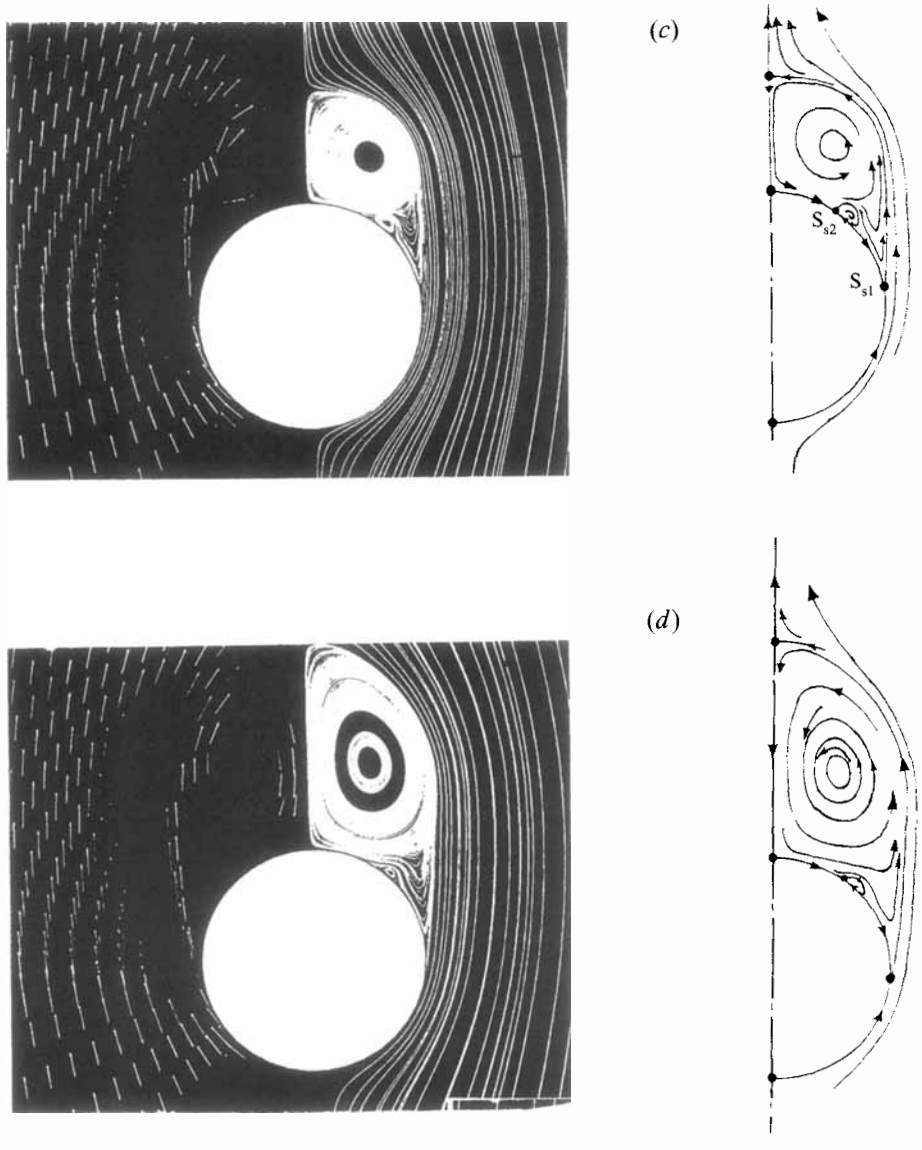

FIGURE 5. Cross-plane flow pattern, $\alpha = 30°$; (*a*) $x/D = 0.48$, (*b*) $x/D = 1.75$, (*c*) $x/D = 3.5$, (*d*) $x/D = 3.75$.

degree thesis by Abazariyan (1995), whose experiment was done in a water channel using a particle seeding technique. Agreement is good.

The nose vortex for $\alpha = 50°$ differs from that for $\alpha = 30°$ in an important way: it extends back to join the core of the primary cylinder separation. This will be discussed in connection with the horseshoe vortex system in §4.4.

3.3.3. *Cross-plane flow pattern*

The cross-plane flow patterns shown in figure 8(*a–e*) appear to be similar to those for 30° incidence, but are more regular over all the downstream region shown. The vortices are larger, as expected for higher incidence. The black core and the black ring will be discussed in §4.5.

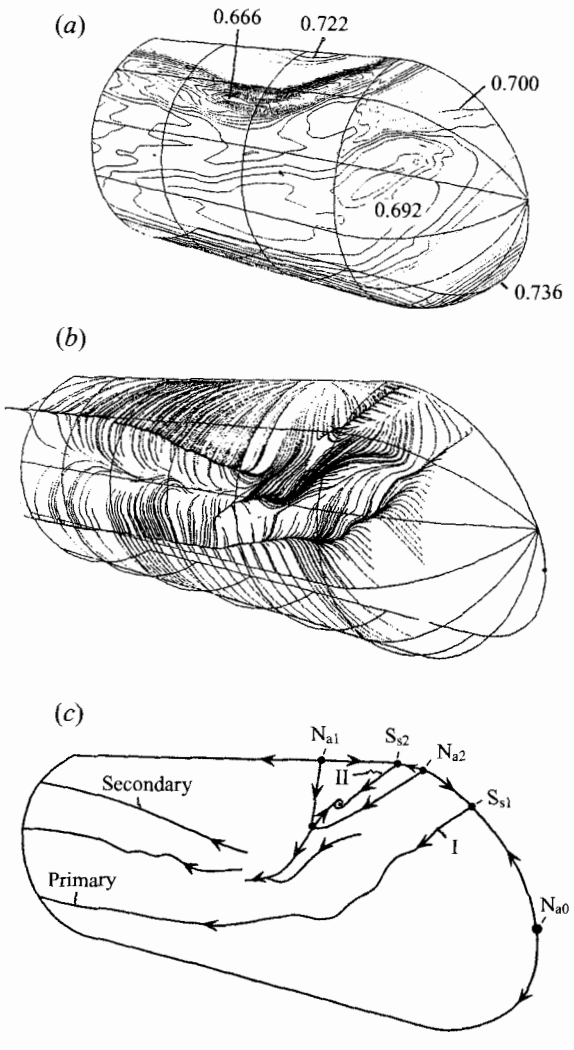

FIGURE 6(*a–c*). For caption see facing page.

4. Highlights of three-dimensional features

In this section, a few aspects peculiar to three-dimensional separated flow structure are selected for special attention.

4.1. *Tornado-like vortices*

The tornado-like vortices are characterized by their axis of rotation being inclined to the body surface. After leaving the body surface, they are quickly bent. From the series of particle traces on the parallel surfaces, at $\alpha = 10°$ and 30°, these vortices in the nose region are seen to bend slightly backward, but more noticeably laterally toward the symmetry-plane. From the symmetry-plane, they are swept downstream.

The significance of this type of vortex in the present context is that it occurs only in three-dimensional flows involving separation. The present authors (1976) briefly discussed this type of vortex before it was further recognized (Wang *et al.* 1990) that such vortices represent a unique feature of three-dimensional separated flows in general. The present calculations capture these vortices in agreement with experiments.

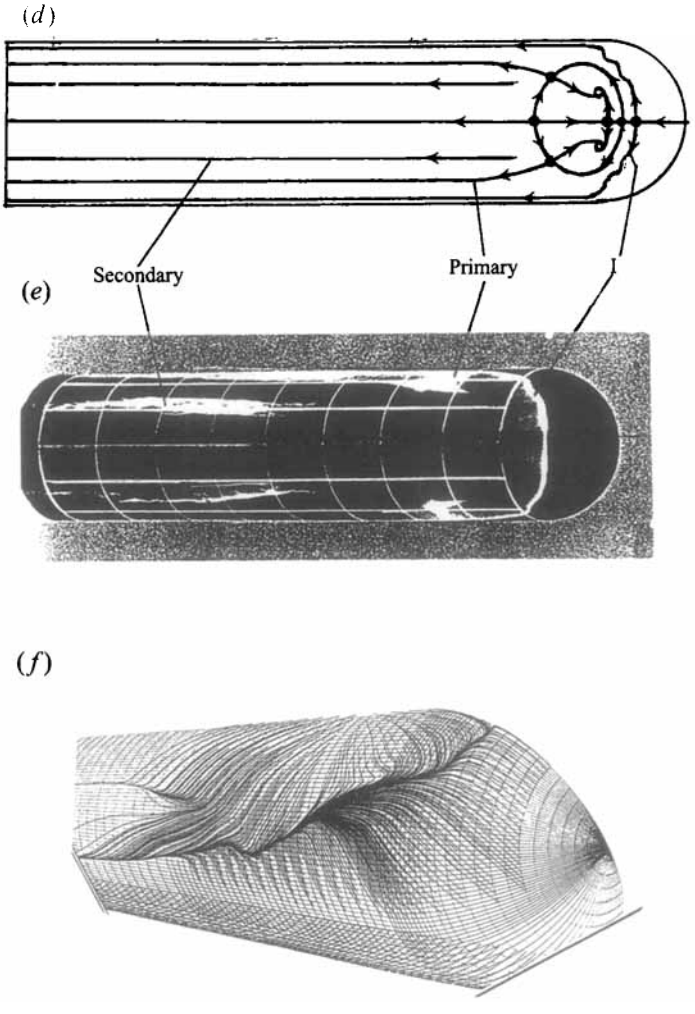

FIGURE 6. Parallel surface flow pattern, $\alpha = 50°$. (*a*) Surface pressure. (*b*) Computed particle traces. (*c*) Topological sketch. (*d*) Redrawing of (*c*). (*e*) Experiment. (*f*) Parallel surface pattern, $k = 4$.

The circumstance under which tornado-like vortices occur was discussed in Wang *et al.* (1990). It was reported there that whenever flows from at least three opposing directions (figure 9*a*) encounter one another on a body surface, such a vortex would develop, except where there is the possibility of a nodal separation point. The latter occurs less often because the opposing flows must balance.

The three-way-encounter pattern ensures the creation of the normal (to the body surface) component of vorticity (figure 9*b*) necessary to sustain such vortices. Clearly a three-way encounter involving opposing flows can only occur in three-dimensional separated regions. The neighbourhood of vortices F_1 and F_2 in figure 3(*c*), for example, fits into this description.

In the nose region, the interaction between such tornado-like vortices and the reversed flow due to separation leads to a complicated twisting structure as in the case of $\alpha = 30°$.

Mathematically, the existence of a tornado-like vortex was predicted by Perry & Chong (1981) in their phase-space topology study. Our present work contributes to

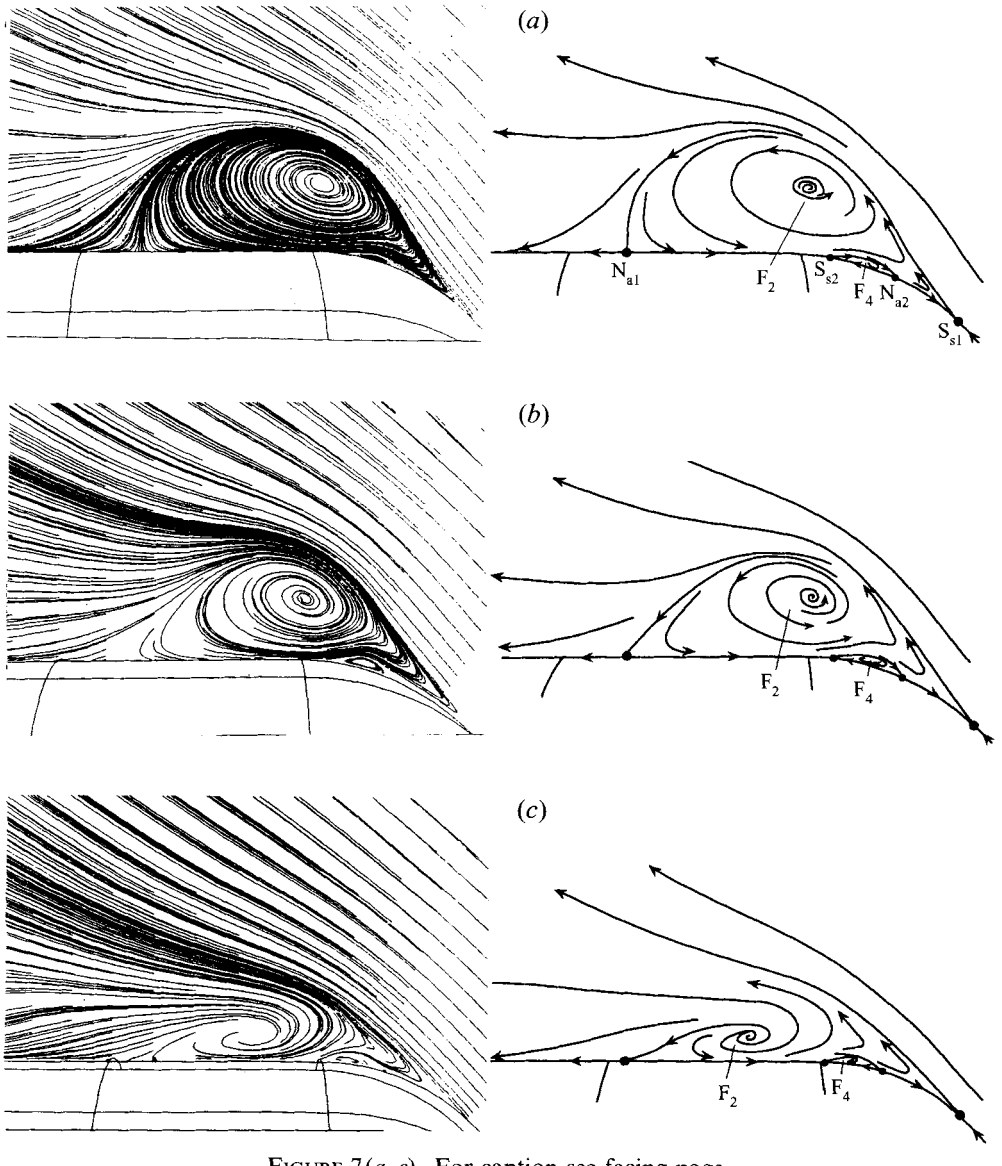

FIGURE 7(*a–c*). For caption see facing page.

shedding light on the physical aspects of this problem, shows the circumstances under which such a vortex would actually occur and provides calculated and experimental examples.

From all cases known so far, tornado-like vortices are observed to be located at the ends of a separation line: F_1 and F_2 of figure 3(*c*) are just such examples. They spiral clockwise or counter-clockwise depending on at which end of the separation line they are located, but they always spiral inward. On spheroids (Wang *et al.* 1990), tornado-like vortices were found to occur even in the middle of a separation line (i.e. cut the latter into segments) because the local flow satisfies the three-way-encounter condition.

Previously we have referred to tornado-like vortices as 'vertical vortices' (Wang *et al.* 1990) and later 'normal vortices' (Wang & Hsieh 1992), because their axis of rotation near the body was thought to be normal to the body surface. However, this

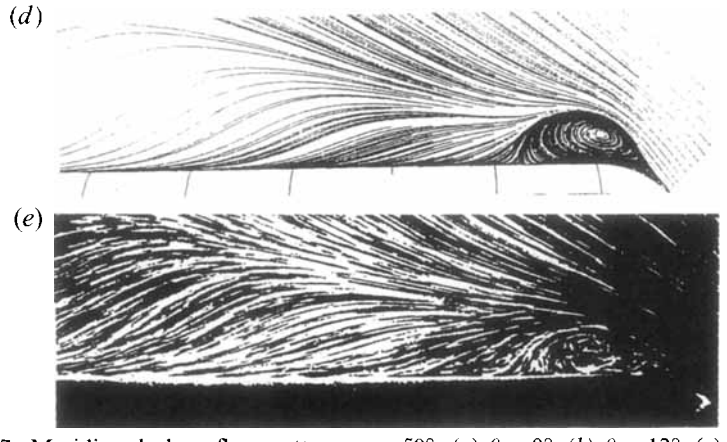

FIGURE 7. Meridional plane flow pattern, $\alpha = 50°$: (*a*) $\theta = 0°$, (*b*) $\theta = 12°$, (*c*) $\theta = 24°$, (*d*) $\theta = 0$ from calculations, (*e*) $\theta = 0$ from experiments.

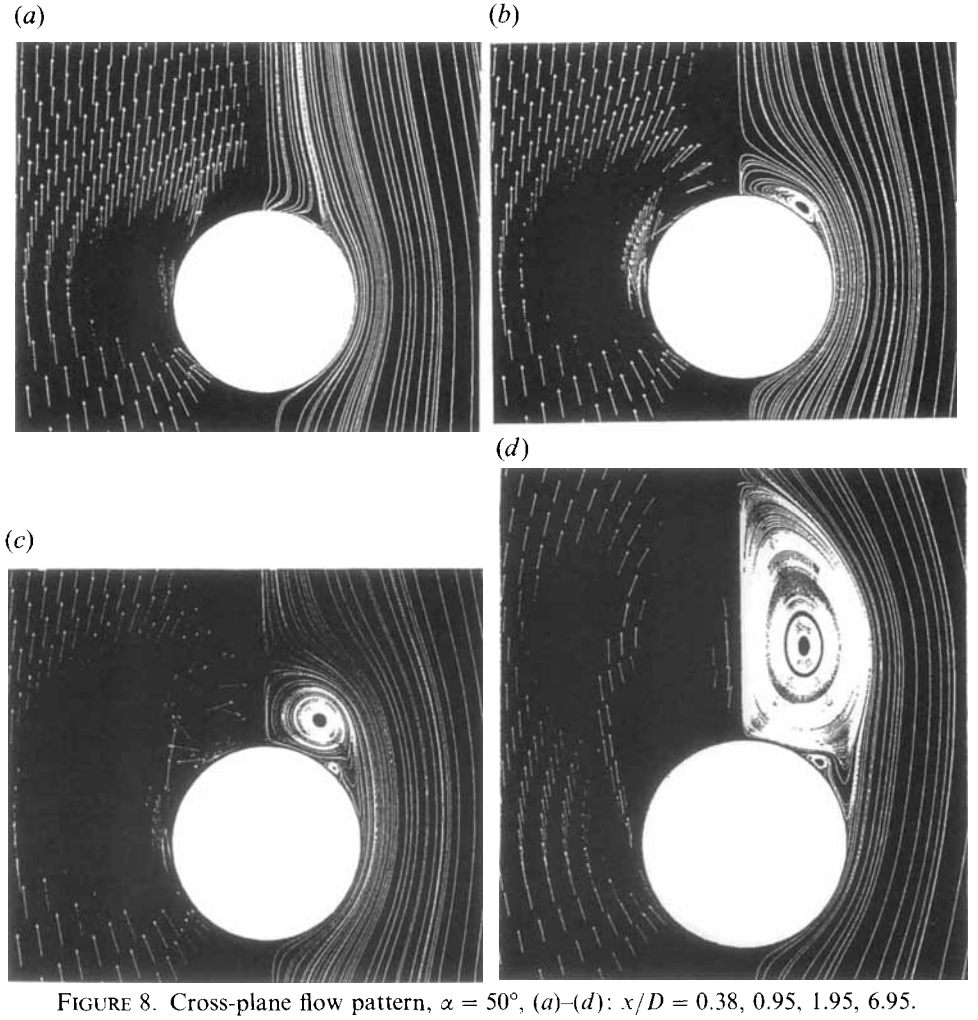

FIGURE 8. Cross-plane flow pattern, $\alpha = 50°$, (*a*)–(*d*): $x/D = 0.38, 0.95, 1.95, 6.95$.

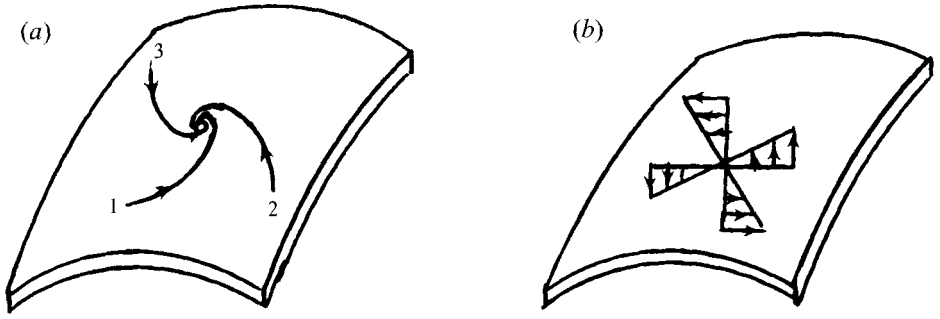

FIGURE 9. (*a*) Normal vortex. (*b*) Normal vorticity.

is not necessarily true: the axis in general is believed to be inclined rather than normal to the body. Some authors also referred to such vortices as 'Werle vortices' because Werle (1962) was thought to be the first who reported these vortices. However, the so-called part-span vortices (Black 1952) on a swept-back wing appear to be also of this same type. Neither is it justifiable to call them 'spiral vortices' because all vortices in three-dimensional flows are generally spiral in nature. Lacking an appropriate label at this time, we simply use the term 'tornado-like vortices' in this paper.

4.2. *Outward-spiralling vortices*

Vortices are commonly pictured as spiralling (or rotating) inward whether clockwise or counter-clockwise. Concrete examples of outward-spiralling vortices have not been reported, at least to the authors' knowledge, until recently (Ying *et al.* 1987; Wang & Hsieh 1992; Zhang & Deng 1992; Visbal & Gordnier 1994). Such vortices cannot exist in two-dimensional flows because of the lack of supply of fluid to maintain mass continuity or because they are unstable, but they can occur in three-dimensional flows because fluid can be supplied laterally. Vortex patterns as seen from either computer plots or experimental photos are usually not clear regarding whether they spiral inward or outward unless carefully examined. In the present investigation, outward-spiralling vortices are seen in the nose separation and the cross-plane patterns for all three cases calculated.

A vortex in a three-dimensional flow can normally spiral either with decreasing or increasing radius. The particle tracing in figure 12(*b*) provides a good example. Such a change of spiral radius generates precisely the inward- or outward-spiral pattern. Therefore, outward spiralling is a natural development in three-dimensional flows; there is no question about the supply of fluid. The reason why a vortex changes its spiral radius can be kinematically seen using the continuity equation (Zhang & Deng 1992; Visbal & Gordnier 1994)

$$\frac{\partial u}{\partial x}+\frac{\partial v}{\partial y}+\frac{\partial w}{\partial z}=0,$$

where Cartesian coordinates are used for simplicity. Assume the main streaming direction is x, then as $\partial u/\partial x$ decreases $\partial v/\partial y+\partial w/\partial z$ must increase. The latter, in turn, would result in an outward-spiral pattern. Similarly, if $\partial u/\partial x$ increases the opposite would occur. In three-dimensional flows, $\partial u/\partial x$ could decrease (i.e. decelerating) or increase (accelerating) according to the local conditions.

Instead of using $\partial u/\partial x$, or $\partial \rho/\partial t+\partial \rho u/\partial x$ if compressible as the deciding parameter, Zhang (1994) derived a criterion in terms of the pressure gradient $\partial p/\partial x$ and Mach number M, through Navier–Stokes equations at very large Reynolds number.

4.3. *Limit-cycle pattern*

The plane limit-cycle pattern was discussed in §3.2.2. Figure 4(*a*) shows the circumstance in which this pattern is formed, namely an outward-spiral flow is enclosed inside an inward-spiral flow. Since outward-spiral flows can only occur in three-dimensional flows, it follows that a plane limit-cycle flow pattern is also peculiar to three-dimensional flows. In §4.5, limit-cycle patterns in the cross-planes will be discussed. There an outward-spiral vortex is located concentrically inside an inward-spiral vortex. In any case, it should be kept in mind that all the cut-planes, whether meridional or cross, are not real stream planes, the only exception being the symmetry-plane where the streamlines are the real physical streamlines.

Whenever $\partial u/\partial x$ changes sign a limit cycle will result. If along the same vortex axis, the sign of $\partial u/\partial x$ changes more than once, multiple concentric limit cycles would appear in the cross-plane. This will be discussed further in §4.5.

4.4. *Horseshoe vortex system*

A horseshoe vortex system as depicted in figure 10(*a*) was reported earlier (Wang *et al.* 1989) based on water-tunnel visualizations at higher incidences. In the present calculations, this feature is most clearly demonstrated in figure 13(*c*). To provide better contrast, this figure is produced in colour to show specifically that the horseshoe vortex system originates from the nose separation (red) over the forebody and trails back through the centre of the primary separation vortex shown by green and purple traces. This is presumably because the primary separation vortex over the cylinder portion of the body is so strong that it entraps the trailing vortex from the nose into its core, so the two combined forge a horseshoe shape.

Photos of horseshoe vortex systems were taken at different incidences during water-tunnel tests, two of them are reproduced here. The one for $\alpha = 50°$ (figure 10*b*) shows clearly the system being originated from the nose region and then entrapped in the core of the primary separation, but figure 10(*c*) for $\alpha = 60°$ exhibits these key features even more convincingly. The nose vortex extension is green in colour, whereas the primary separation is shown by the dye injections alternately in red and green. In experiments, vortex bursting occurred. This is why the system does not extend back very far as the computer plot (figure 13*c*) shows. Again, figure 10(*b*, *c*) is presented in colour to provide better visualization.

4.5. *Coaxial counter-spiralling vortices*

In figures 5 ($\alpha = 30°$) and 8 ($\alpha = 50°$) for the cross-plane patterns, black cores and black rings were seen. The meaning of these two features is explained here. To see the detailed structure of the cross-plane patterns, particle tracings were made at a number of the cross-stations. Two examples of the results are shown in figure 11(*a*) for $\alpha = 30°$ at $x/D = 3.50$ and in figure 11(*b*) for $\alpha = 50°$, at $x/D = 1.25$. In both figures 11(*a*) and (*b*) tracings were started from a point A farther away from the centre and point B closer to the centre. It is seen that the one starting from B spirals outward and the one starting from A spirals inward, and both are clockwise; they approach a limit cycle from opposite sides.

Note that the white ring and core in figure 11(*a*) correspond to the black ring and core in figures 5 and 8 due to the difference in the background light.

The limit cycle in figure 11(*b*) is clearly defined. In figure 11(*a*), the two tracings do not directly approach a common limit cycle; instead they are separated by a white ring. There are, in fact, two limit cycles. In the phase-plane theory of nonlinear dynamics (Thompson & Stewart 1987), these limit cycles are classified as stable limit cycles.

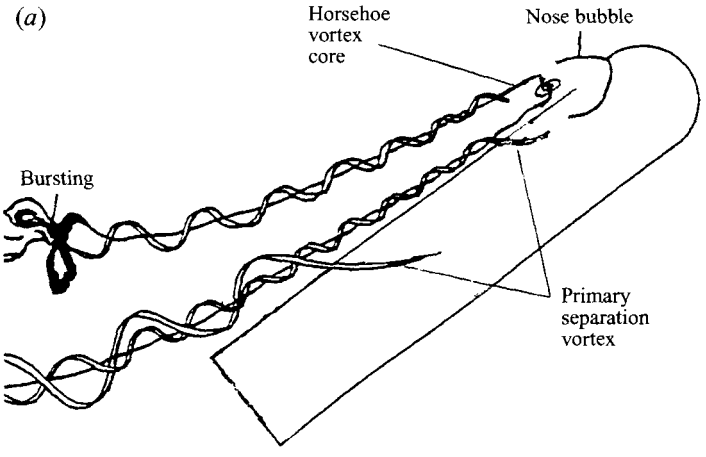

FIGURE 10(*a*). For caption see facing page.

Within the white ring, there is an unstable limit cycle (figure 11*c*) which divides the white ring area into two: the outer part approaches the outer stable limit cycle whereas the inner part approaches the inner stable limit cycle. This structure could have been revealed if particle traces were started inside the white ring.

The multiple limit-cycle structure in the cross-planes just presented agrees with the conceptual prediction of Zhang & Deng (1992), who specifically depicted that as the sign of $\partial u/\partial x$ (see §§4.2, 4.3) continues to change periodically along the same vortex axis, concentric stable and unstable limit cycles will be alternately formed. A change of positive $\partial u/\partial x$ to negative $\partial u/\partial x$ results in a stable limit cycle, whereas the reverse leads to an unstable limit cycle.

The black core in figures 5 and 8 is believed to result from numerical error. The plot program itself is only second order in accuracy, and it is not accurate enough to plot in the small core area. A similar black core has been found by other researchers also.

4.6. *Particle traces in the nose region*

Particle traces were made to understand how the fluid particles go in and out of the nose separation region and how they move inside. Two examples are given here.

Figure 12(*a*) for 30° incidence shows that three particles start from the free stream, enter the nose separation region, spiral generally toward the symmetry-plane and then escape downstream. The traces tend to tangle and lack a consistent trend. This could be influenced by the bending of the tornado-like vortices.

In figure 12(*b*) for 50° incidence, a particle starts inside the nose region, spirals first clockwise inward and then counter-clockwise outward as it travels toward the symmetry-plane. Upon approaching the symmetry-plane, the velocity normal to the symmetry-plane must be gradually decreased to zero because an opposite flow arrives from the other side of the symmetry-plane, thus according to the kinematic argument in §4.2, an outward-spiral vortex pattern naturally follows. The pattern of figure 12(*b*) is less tangled than that of figure 12(*a*), presumably because of the absence of tornado-like vortices.

From a number of similar traces, including some not shown here, the following observations can be made. (i) Particles generally spiral toward the symmetry-plane and then back away from it before going out; some even shift back and forth more than once. The axis of rotation for such spiral motion is more or less normal to the

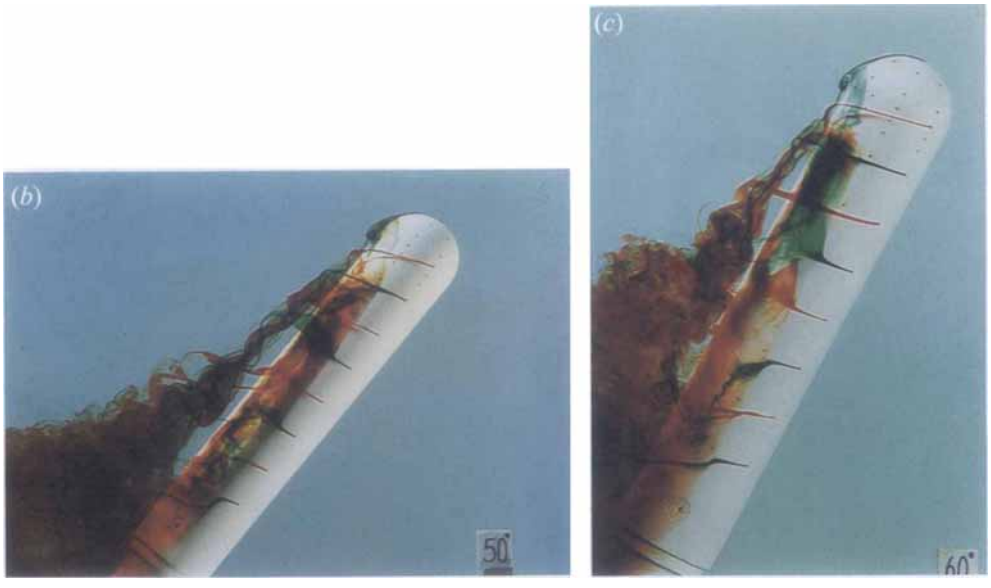

FIGURE 10. Horseshoe vortex pattern: (*a*) schematic, (*b*, *c*) experiments: (*b*) $\alpha = 50°$, (*c*) $\alpha = 60°$.

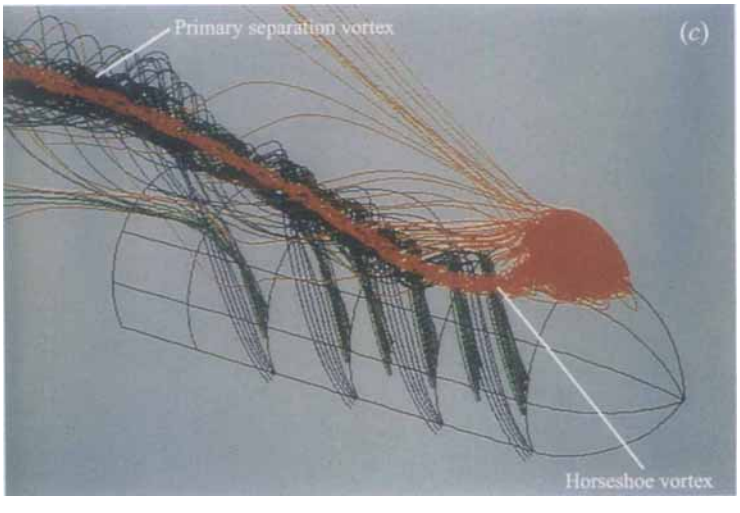

FIGURE 13(*c*). For caption see page 106.

symmetry-plane. The resulting vortex pattern can be referred to as transverse vortices in contrast to the tornado-like vortices as discussed above. (ii) Particles spiral more turns for the 50° incidence than for the 30° incidence, indicating stronger vortical motion. The total number of turns is surprisingly large. (iii) Some of the particles for 50° incidence do not leave the nose region to enter the downstream wake, instead they turn sideways to start forming a horseshoe vortex system.

The traces shown here suggest a much more complex structure than would be expected. Our investigation of this particular aspect is limited; it only serves to shed some further light but is unable to offer a complete explanation. At present, there is no experiment or similar calculation to compare with.

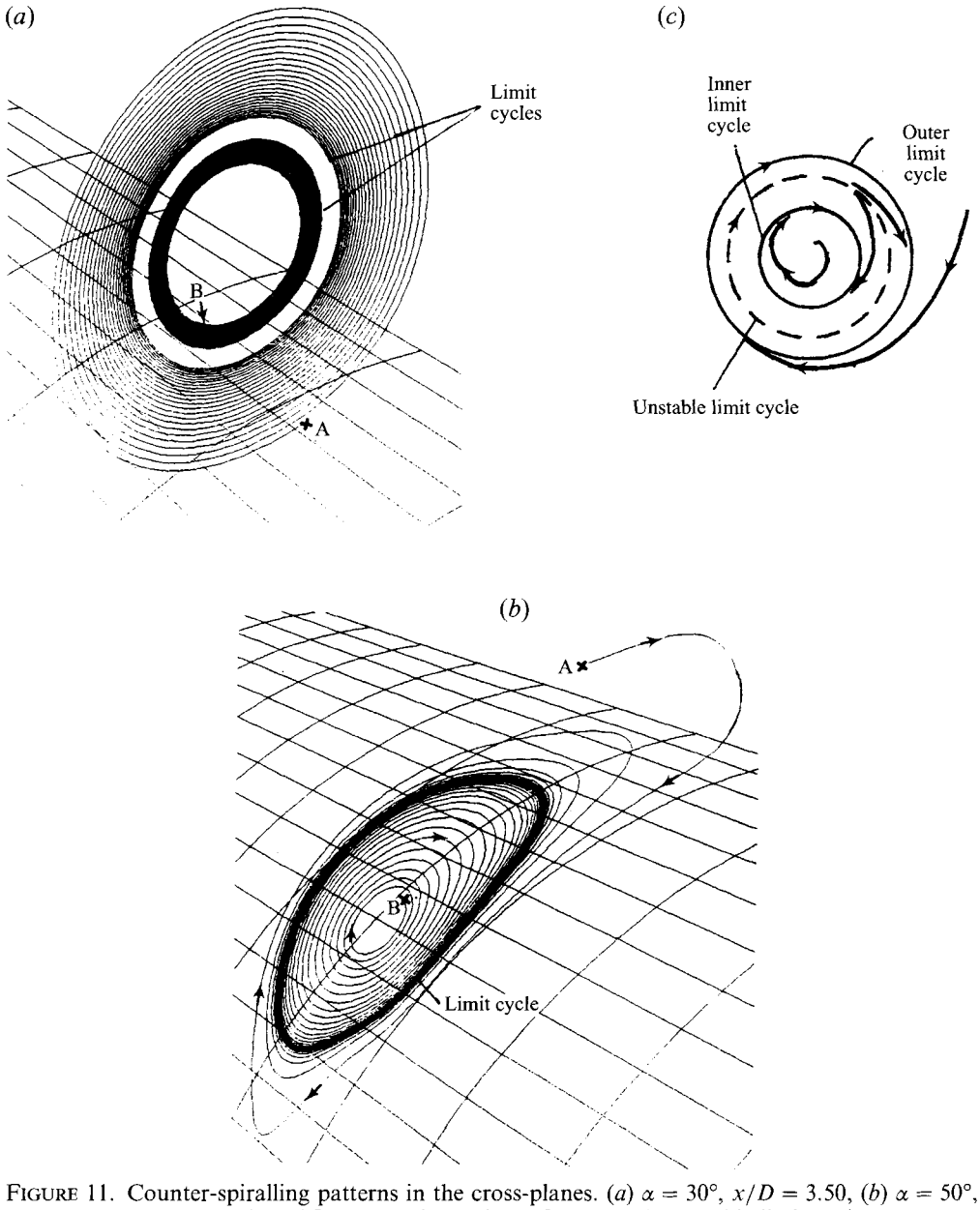

FIGURE 11. Counter-spiralling patterns in the cross-planes. (*a*) $\alpha = 30°$, $x/D = 3.50$, (*b*) $\alpha = 50°$, $x/D = 1.25$. A and B are starting points of traces. (*c*) Unstable limit cycle.

4.7. *Overall flow pattern*

Figure 13(*a–c*) presents computer traces of the overall patterns (figure 13*c* is shown on page 103). While the results presented in §3 are all two-dimensional, the particle traces here offer genuine three-dimensional views. In all three cases, the flow separates at the front nose. This nose separation becomes stronger as incidence increases. For $\alpha = 10°$ and 30°, fluid leaves the nose separation and most immediately enters the downstream wake, but part is entrapped into the primary cylinder separation vortex at different stations. For $\alpha = 50°$, the nose separation vortex first extends out and then turns back to be entrapped in the core of the primary separation, forming a horseshoe

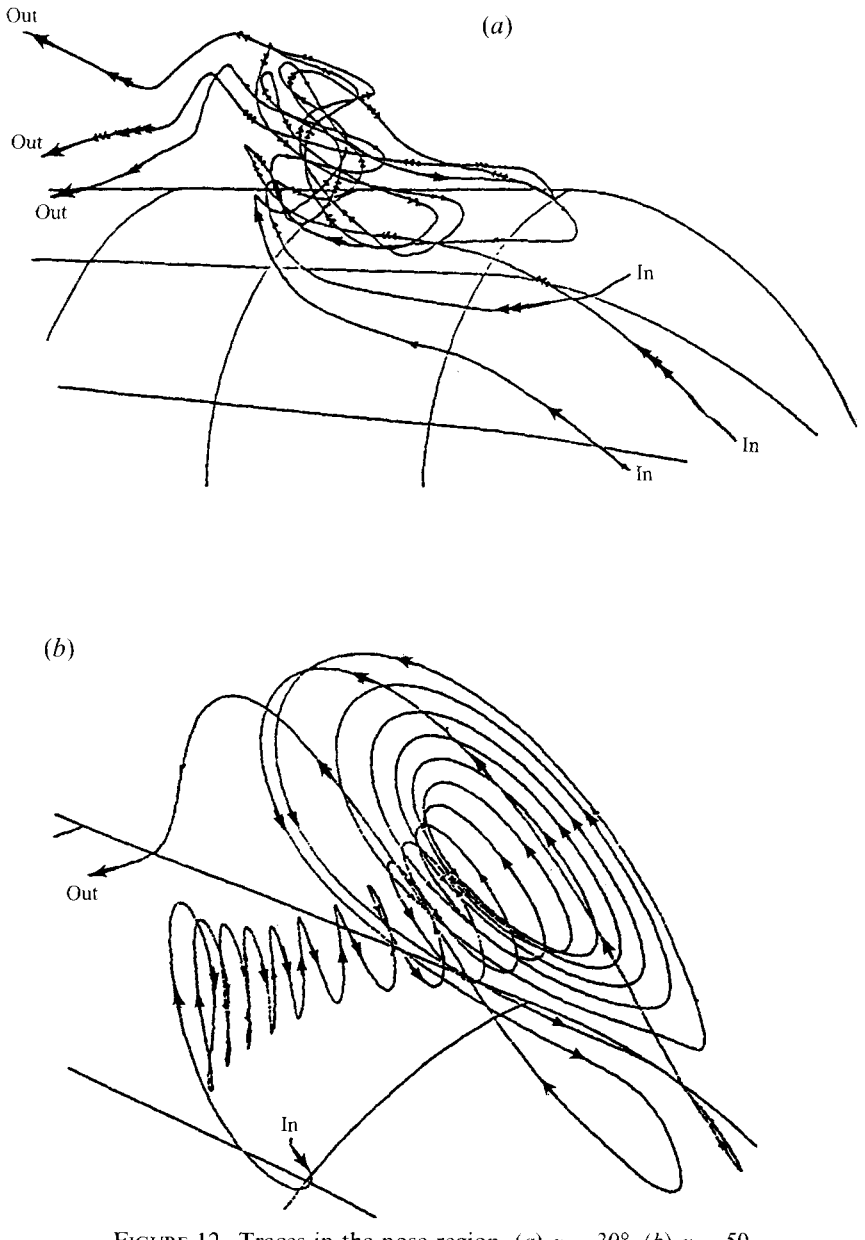

FIGURE 12. Traces in the nose region. (*a*) $\alpha = 30°$, (*b*) $\alpha = 50$.

vortex system above the body. Many traces around the trailing vortex show that as they spiral downstream, their radius may continuously change, exhibiting an inward- or outward-spiral pattern.

The primary separation over the cylinder portion starts at the rear end, grows stronger and extends forward at increasing incidence. Whereas the nose separation is basically a separation of meridional flow, the primary and secondary separation over the cylinder is largely the cross-flow separation.

At $\alpha = 10°$ and $30°$, the nose separation is not connected to the primary separation so the overall separation near the body surface is classified as an open separation, meaning that the upstream surface flow can reach the back of the nose separation,

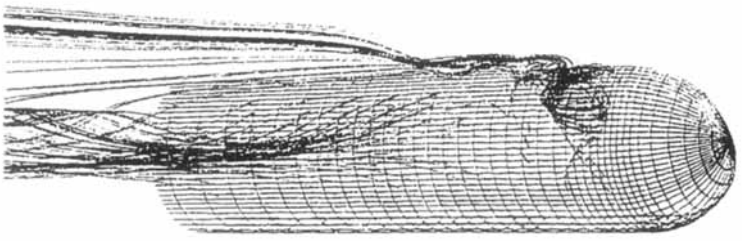

(*a*)

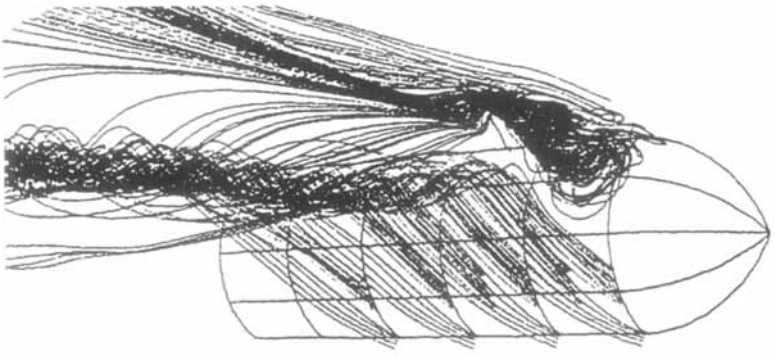

(*b*)

FIGURE 13. Overall flow pattern: (*a*) $\alpha = 10°$, (*b*) $\alpha = 30°$, (*c*, page 103) $\alpha = 50°$.

whereas at $\alpha = 50°$, the separation is closed so that the surface flow cannot enter the separated region across the surface separation line. This change of separation between open and closed types confirmed the separation sequence proposed by the authors earlier (Hsieh & Wang 1976) on the basis of experimental observations.

In this problem it is noted that three different kinds of vortices coexist, namely tornado-like, transverse and longitudinal (or axial or streamwise) vortices characterized respectively with their axis of rotation being inclined to the body surface, transverse to the symmetry-plane and more or less aligned with the streamwise direction. The last occurs on the cylinder as the primary and secondary separation vortices. The first two occur in the nose region. The simultaneous presence of these two kinds of vortices in the small nose region greatly complicates the flow structure there. All the vortices are three-dimensional in nature, and they spiral inward or outward in the nose separated region or the cylinder separated region.

5. Conclusions

The thin-layer Navier–Stokes equations have been employed in computing the incompressible flow over a hemisphere–cylinder from a compressible code. Results for three incidence angles of 10°, 30° and 50° are obtained.

The detailed separated flow structure on the parallel surfaces, meridional-planes and cross-planes have been presented here together with three-dimensional traces. The surface separation patterns and the appearance of a horseshoe vortex system have been compared with experimental visualizations and agreement is very good even for some detailed features.

The results confirm the systematic separation trend with incidence as previously reported by the authors (Hsieh & Wang 1976; Wang *et al.* 1989). At low incidence ($\alpha = 10°$), there is nose separation accompanied by a pair of vortices, and the primary separation over the cylinder starts at $x/D \approx 2.25$. Secondary separation does not occur until the very rear end. At $\alpha = 30°$ the nose separation becomes the most complicated. There are multiple stages of separation and a large number of vortices. The primary separation over the cylinder extends too close to the nose separation but is still not directly connected. Meanwhile, the secondary separation over the cylinder starts at $x/D \approx 1.7$. Both the primary and secondary separations are of the open type. At $\alpha = 50°$, the separation over the cylinder is finally connected to the nose separation so the overall primary separation becomes the classically closed type. The secondary separation, however, remains open.

A number of structural features unique to three-dimensional separated flows are noted; some were reported recently from water-tunnel visualizations, but confirmed by the present calculations, other are new. These include the tornado-like vortex, outward-spiral vortex, horseshoe vortex system, coaxial counter-spiral vortices and limit cycles. Some of these features are not wholely understood and require further investigation.

The CRAY YMP/C90 computing time for all the computations was provided by the NASA User Program. The authors are indebted to one of the reviewers for suggesting the interpretation of the black ring and to C. M. Hung and S. X. Ying for their comments.

REFERENCES

ABAZARIYAN, M. 1995 Visualization of laminar cross-plane and meridional-plane structure above an inclined hemisphere-cylinder. Masters thesis, San Diego State University, CA.

BLACK, J. 1952 A note on the vortex pattern in the boundary layer flow of a swept-back wing. *J. R. Aero. Soc.* **56**, 279–285.

HOANG, N. T., REDINIOTIS, X. & TELIONIS, D. T. 1991 Separation over axi-symmetric bodies at large angles of attack. *AIAA Paper* 91-0277.

HOANG, N. T., TELIONIS, D. T. & JONES, G. S. 1990 The hemisphere-cylinder at an angle of attack. *AIAA Paper* 90-0050.

HSIEH, T. 1976 An investigation of separated flow about a hemisphere-cylinder at 0–19-deg. incidence in the Mach number from 0.6 to 1.5. *Tech. Rep.* 76-112. Arrnold Engineering Development Center.

HSIEH, T. 1977 Low supersonic flow over hemisphere-cylinder at incidence. *J. Spacecraft Rockets* **14**, 662–668.

HSIEH, T. 1981 Calculation of viscous sonic flow over hemisphere-cylinder at 19 degree incidence: the capturing of nose vortices. *AIAA Paper* 81-0189.

HSIEH, T. & WANG, K. C. 1976 Concentrated vortex on the nose of an inclined body of revolution. *AIAA J.* **14**, 698–700.

KORDULLA, W., VOLLMERS, H. & DALLMANN, U. 1986 Simulation of three-dimensional transonic flow with separation past a hemisphere-cylinder configuration. *AGARD CPP*-412, paper 31.

PERRY, A. E. & CHONG, M. S. 1981 A description of eddying motions and flow patterns using critical-point concepts. *Ann. Rev. Fluid Mech.* **19**, 125–155.

PULLIAM, T. H. & STEGNER, J. L. 1980 Implicit finite difference simulation of three-dimensional compressible flow. *AIAA J.* **18**, 159–167.

ROE, P. L. 1981 Approximate Riemann Solvers, parameter vectors and difference schemes. *J. Comput. Phys.* **43**, 357–372.

THOMAS, J. L., KRISH, S. T. & ANDERSON, W. K. 1990 Navier–Stokes computations of vortical flows over low aspect ratio wings. *AIAA J.* **28**, 205–212.

THOMSON, J. M. T. & STEART, H. B. 1987 *Nonlinear Dynamics and Chaos*, p. 63. John Wiley & Sons.

TOBAK, M. & PEAKE, D. J. 1982 Topology of three-dimensional separated flows. *Ann. Rev. Fluid Mech.* **14**, 61–85.

VAN LEER, B., THOMAS, J. L., ROE, P. L. & NEWSOME, R. W. 1987 A comparison of numerical flux formulas for Euler and Navier–Stokes equations. *AIAA Paper* 87-1104-cp.

VISBAL, M. R. & GORDNIER, R. E. 1994 Crossflow topology of vortical flows. *AIAA J.* **32**, 1085–1087.

WALATKA, P. P., BUNING, P. G., PIERCE, L. & ELSON, P. A. 1990 PLOT3D User's Manual. *NASA TM*-101067.

WANG, K. C. 1976 Boundary layer separation in three dimensions. In *Proc. Lockheed-Georgia Company Viscous Flow Symposium*, pp. 341–414.

WANG, K. C. & HSIEH, T. 1992 Separation pattern and flow structure about a hemisphere-cylinder at high incidence. *AIAA Paper* 92-2712.

WANG, K. C., HU, C. H. & ZHOU, H. C. 1989 The separated flow structure over an inclined hemisphere-cylinder. *Rep. AE & EM* TR-89-02. San Diego State University, San Diego, CA.

WANG, K. C., ZHOU, H. C., HU, C. H. & HARRINGTON, S. 1990 Three-dimensional separated flow structure over prolate spheroids. *Proc. R. Soc. Lond.* A **429**, 73–90.

WERLE, H. 1962 Separation of axisymmetric bodies at low speed. *La Recherche Aero.* **90**, 3–14.

YING, S. X., SCHIFF, L. B. & STEGER, J. L. 1987 A numerical study of three-dimensional separated flow past a hemisphere cylinder. *AIAA Paper* 87-1207.

YING, S. X., STEGER, J. L., SCHIFF, L. B. & BAGANOFF, D. 1986 Numerical simulation of unsteady viscous high-angle-of-attack flows using a partially flux-split algorithm. *AIAA Paper* 86-2179.

ZHANG, H. X. 1994 Topological analysis of vortex motion. *Rep. China Aerodynamics Center, Sichuan, PRC* (in English).

ZHANG, H. X. & DENG, X. G. 1992 Analytical studies for three-dimensional steady separated flows and vortex motion. *ACTA Aerodynamics SINICA* 10, 1 (in Chinese).